Bistatic Localization of Objects in Very Shallow Water

TING ZHANG[1,2], T. C. YANG [ID][1,3], AND WEN XU [ID][1,3], (Senior Member, IEEE)
[1]College of Information Science and Electronic Engineering, Zhejiang University, Hangzhou 310027, China
[2]Zhejiang Provincial Key Laboratory of Information Processing, Communication and Networking, Hangzhou 310027, China
[3]Zhejiang Provincial Key Laboratory of Ocean Observation-Imaging Testbed, Zhoushan 316021, China

Corresponding author: T. C. Yang (tsihyang@gmail.com)

ABSTRACT Bistatic or multi-static systems use spatially distributed sources and/or receivers to ensonify scattering objects over a distance to obtain the acoustic images of individual targets for classification purposes. The targets need to be localized first and separated from the clutter. To reach targets at a distance, low frequency sound is often used; targets can in principle be classified based on the frequency and azimuthal angle response of the echo return, referred to as acoustic color. Practical application of this technology is limited by the array size and the ability to localize the target and extract the scattering echo. Deconvolution of conventional beamforming (CBF) has been shown to achieve a narrow beam width and low side lobe levels equivalent to CBF of an array of much larger aperture. This method is applied to active sonar in this paper. Analysis of simulated and tank experimental data demonstrated a better separation of targets and a higher target-to-reverberation ratio than that using CBF.

INDEX TERMS Localization, beamforming, deconvolution, horizontal array.

I. INTRODUCTION

Underwater imaging technology has wide applications in ocean exploration and other fields, such as pipe and cable survey, bridge pillar inspection, fish detection, mine classification, etc. In very shallow (say ≤ 30 m) or shallow water (≤ 100 m), detection and classification of bottom laid (proud, partially/completely buried) objects presents a challenging problem to the mine countermeasures (MCM) community that requires a novel solution [1]–[4]. Due to the shallow water depth, sound interactions with the bottom induce complex multipath arrivals and high level reverberation returns.

Optical imaging can be used to observe and discriminate objects within the water column. It provides superior resolution but is limited to short ranges depending on the water condition. Compared with optical imaging, underwater acoustic imaging covers a much longer range. Classical MCM sonar systems operate at high frequencies, e.g., tens to hundreds kilohertz, and use array beamforming to provide fine resolutions for the acoustic image. The detection range is

often limited (<50-100 m) due to the high propagation loss of high frequency sound. As a result, it will take days to weeks to survey a large operation area, which is unacceptable for many practical situations. Low frequency (e.g., 20 kHz or less) sonar has been recently proposed to extend the detection range to hundreds-to-thousands meters. It thus could provide a high rate for target detection over a large area. (A high area coverage rate is a critical consideration for operational MCM.) In addition, low frequency sound penetrates deeper into sediments, permitting detection of partially and completely buried munitions.

Acoustic imaging uses an active sound to ensonify scattering objects over a distance. The corresponding scattered returns are recorded by the receivers in either monostatic, bistatic or multistatic mode to detect, localize and classify the objects of interest. Modern active sonar uses narrow beams to ensonify the target and separate the target from reverberation and clutter. Given practical constraints on the array aperture, acoustic returns at low frequencies may not provide a clear image of the target as the image resolution decreases with decreasing frequency and increasing range, different types of targets can still be distinguished based on

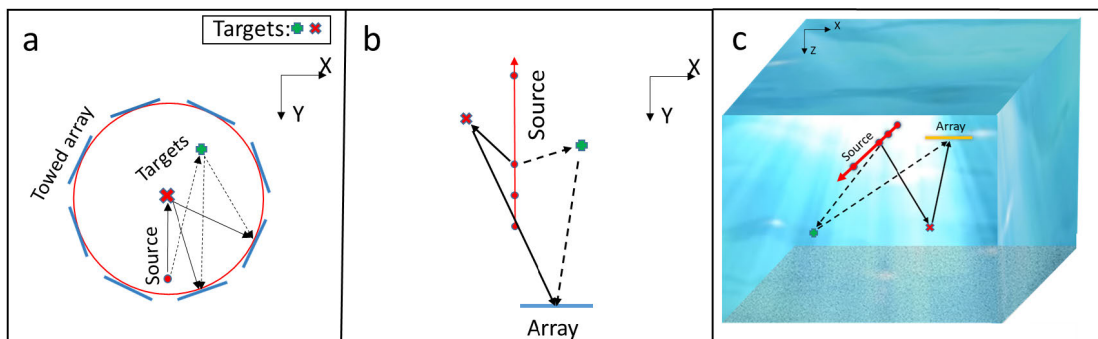The associate editor coordinating the review of this manuscript and approving it for publication was Ki-Hong Park [ID].

FIGURE 1. (a) Top view of the geometry of a fixed source, targets, and towed HLAs and (b) a fixed array, targets, and a moving source, (c) is the profile view of the geometry in Fig. 1(b).

the frequency and (azimuthal) angle response of the echo return, referred to as acoustic color [5]–[12]. To extract the acoustic color, the target needs to be localized and separated from the strong reverberation return. This requires a beamformer that produces a narrow beam width. (The acoustic color image can then be reconstructed by deconvolving the channel impulse response from the echo return.) To ensure the quality of the acoustic color reconstruction, the beamformer must produce low level sidelobes so that minimum energy is leaked from the reverberation/clutter to the echo return. Furthermore, to obtain a wide angular coverage, multiple sources and/or receivers spatially distributed over the area of interest (referred to as multi-static sonar) are often needed particularly for a moving target. For fixed objects, such as mines, moving source and/or receivers can be used, trading time for spatial coverage, referred to as bistatic scattering.

Acoustic responses of various objects have been studied in the literature [1]–[4], [13]–[7] to illustrate the use of acoustic color. Monostatic [13] and bistatic [14] acoustic scattering returns of various objects were measured in a tank. Similar measurements were carried out in a pond to investigate the frequency and azimuth responses of a single target [15] and multiple targets [16] for underwater unexploded ordnance (UXO) applications. Bistatic detection and classification of bottom laid, partially and fully buried objects were carried out in very shallow water (VSW) using a rack-mounted horizontal line array (HLA) and/or an array mounted on an autonomous underwater vehicle (AUV) as the receiver [1]–[4]. The AUV technology provides an opportunity for extended three-dimensional angular coverage of the target return due to its mobility for target detection and classification [17]. Since an AUV mounted or towed array is limited in its size due to the payload constraint of the vehicle, synthetic aperture beamforming was used to improve the direction of arrival (DOA) estimation of the target echo, and suppress the sidelobes (to avoid masking of the target and false alarms created by reverberation return). For a rack mounted system, synthetic aperture beamforming has proven its usefulness taking advantage of the accurately known (source/receiver) positions. For the AUV mounted/towed

array, the performance of synthetic aperture beamforming for target localization is highly dependent on accurate platform navigation and timing, which is used to determine the array element positions (as a function of time). Any position error (between different pings) will seriously affect the performance of synthetic beamforming [1]–[4]. In this paper, instead of synthetic aperture beamforming, we propose deconvolved conventional beamforming (CBF) [18] for object (mine) localization. Previous work has shown that deconvolution applied to CBF [18] can yield a fine beam and low level sidelobes equivalent to CBF of an array with many ($\sim$10) times larger aperture. In this work, deconvolved CBF is applied to active sonar. Each ping is used to estimate the target DOA and target's range from the array using CBF and then deconvolution. It is shown that deconvolution produces a sparse map of targets and clutter. Targets and clutter are (better) separated in space by applying deconvolution to multiple pings (than not). Target-to-reverberation ratios using deconvolved CBF are significantly higher than that using CBF ($\sim$10 dB for the data analyzed).

Two source-receiver configurations are as shown in Fig. 1 to illustrate potential system concepts. In Fig. 1(a), a low-frequency source is used to ensonify the VSW seabed from off-shore. An AUV or unmanned surface vehicle is used to tow a HLA around the perimeter of the ensonified area to detect and localize the targets within the area similar to that discussed in [1]–[4]. In Fig. 1(b) and (c), a fixed (bottom deployed) HLA is used and a moving source (an AUV) projects sound at different positions to obtain different bistatic angles similar to the geometry used in the tank experiment discussed below.

This paper is organized as follows. Section II reviews the field scattered by targets in a waveguide, and details the method to localize the target using a HLA of receivers. Section III presents simulation results. Experimental data collected in a tank experiment are analyzed in Sec. IV to localize two different targets. Section V gives the conclusion.

[A comment is in order here. Localization in this paper means estimation of the target's horizontal position, ignoring the target depth information. There exist many methods to

estimate the target depth given a vertical line array, such as matched field processing [19], back propagation [20], and time reversal mirror [21], [22]. Depth localization will not be covered here.]

II. PROBLEM FORMULATION

In a range independent environment, the bistatic pressure at frequency ω from the source to the target and then to the receiver can be expressed in terms of normal modes as [23]

$$p(\overleftarrow{r}, z_r; \omega) = 2\pi\rho(\omega) \sum_{n=1}^{M} \sum_{m=1}^{M} \frac{e^{-ik_m r_{st}}}{\sqrt{k_m r_{st}}} \phi_m(z_s)\phi_m(z_t)$$
$$\times \Omega(\theta_m, \phi_{in}; \theta_n, \phi_{out}) \frac{e^{-ik_n r_{tr}}}{\sqrt{k_n r_{tr}}} \phi_n(z_t)\phi_n(z_r), \tag{1}$$

where $\rho(\omega)$ is the source spectral density; z_s, z_t, and z_r denote the depth of the source, target and receiver respectively; r_{st} and r_{tr} denote the respective ranges from the source to the target and from the target to the receiver; k_m and k_n are the respective wavenumbers of the normal modes of the incoming and outgoing (scattered) signals; $\phi_m(z)$ denotes the m-th mode depth function; and $\Omega(\theta_m, \phi_{in}; \theta_n, \phi_{out})$ is the coupling matrix between the incident and outgoing modes given by

$$\Omega(\theta_m, \phi_{in}; \theta_n, \phi_{out})$$
$$= (1/2k) \left[S_{mn}^+ - S_{mn}^+ \frac{\phi_m'(z_t)\phi_n'(z_t)}{\gamma_m\phi_m(z_t)\gamma_n\phi_n(z_t)} \right], \tag{2}$$

with the following definition

$$S_{mn}^{\pm} = S(\theta_m, \phi_{in}; \theta_n, \phi_{out}) \pm S(\theta_m, \pi - \phi_{in}; \theta_n, \phi_{out}). \tag{3}$$

In (2) and (3), $\gamma_m = \sqrt{k^2 - k_m^2}$ is the vertical wavenumber of the modes, $\phi_m'(z)$ denotes the derivative of the mode depth function with respect to z, and $S(\theta_m, \phi_{in}; \theta_n, \phi_{out})$ is the scattering function of the object (in free space), which is dependent on the incident azimuthal angle ϕ_{in} and the outgoing azimuthal angle ϕ_{out} as well as the incident grazing angle associated with the m-th mode θ_m, and the outgoing grazing angle associated with the n-th mode θ_n. The mode wavenumber and depth functions and the scattering function are a function of frequency which was not explicitly denoted in the above equations.

When the target is at far field, the (incoming and outgoing) dominant modes travel at low grazing angles (e.g., $< 10°$) with a small angular span $\Delta\theta$. We assume that the target's scattering function can then be approximated by that at the mean grazing angle, $S(\theta_m, \phi_{in}; \theta_n, \phi_{out}) \simeq S(\bar{\theta}_m, \phi_{in}; \bar{\theta}_n, \phi_{out}) \equiv S(\phi_{in}, \phi_{out})$ as proposed in [24]. (Henceforth, the grazing angle dependence of the scattering function will be suppressed.) Equation (1) can then be expressed in the form of products of channel transfer functions and scattering function as,

$$p(\overleftarrow{r}, z_r; \omega) = 2\pi \frac{\rho(\omega)}{k} \left[\sum_{m=1}^{M} \frac{e^{-ik_m r_{st}}}{\sqrt{k_m r_{st}}} \phi_m(z_s)\phi_m(z_t) \right.$$
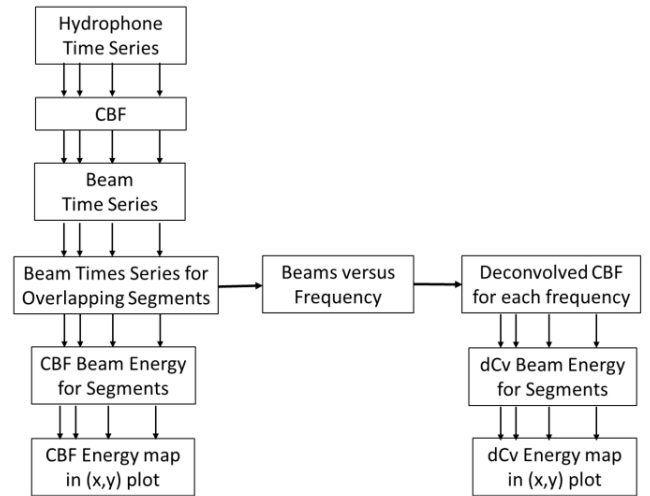

FIGURE 2. Flow chart of data processing.

$$\left. \times S(\phi_{in}, \phi_{out}) \left[\sum_{n=1}^{M} \frac{e^{-ik_n r_{st}}}{\sqrt{k_n r_{st}}} \phi_n(z_t)\phi_n(z_r) \right] \right.$$
$$\equiv \frac{\rho(\omega)}{k} H(r_{st}, \omega) S(\phi_{in}, \phi_{out}) H(r_{tr}, \omega), \tag{4}$$

where $H(r_{st}, \omega) = \sum_{m=1}^{M} \sqrt{\frac{2\pi}{k_m r_{st}}} \phi_m(z_s)\phi_m(z_t)e^{-ik_m r_{st}}$ is the channel transfer function. Equation (4) has been shown to be valid under many conditions, such as when the object size L satisfies $\Delta\theta < \lambda/4L$, where λ is the wavelength [24]. Equation (1) is referred as the wave-theoretical model of object scattering and (4), expressed in dB, is referred to as the sonar equation [24]. Equation (4) will be used to generate simulated data in this paper. (Cf. Sec. III.)

For either simulated or experimental data, the data on the HLA are processed as follows. For each ping, the signal from the source, scattered by the target, and received on the HLA are matched filtered, beamformed by delay and sum (or equivalently beamformed in the frequency domain) to produce time series for each beam. One searches the beam power time series for peaks as a function of delay time and azimuthal angle. The result yields a candidate map of targets and clutter as a function of range and azimuth which can be transformed into a map in the Cartesian coordinate {x, y}. The maps over different pings, as the source or receiver moves over different positions, are summed to produce the final map. In practice, one may search only beam power with sufficient delay time to avoid areas with heavy reverberation returns and beams away from endfire directions to avoid beam splitting due to vertical multipaths. The processing steps are given in Fig. 2; the details are discussed below and illustrated by examples in Sec. III and IV.

Two issues arise for target localization. First, for each ping, it is noted that the map resolution is on the order of $cr\Delta\phi/2B$, where r is the range of target/clutter to the array and B is the bandwidth of the signal. The 3 dB beamwidth for a
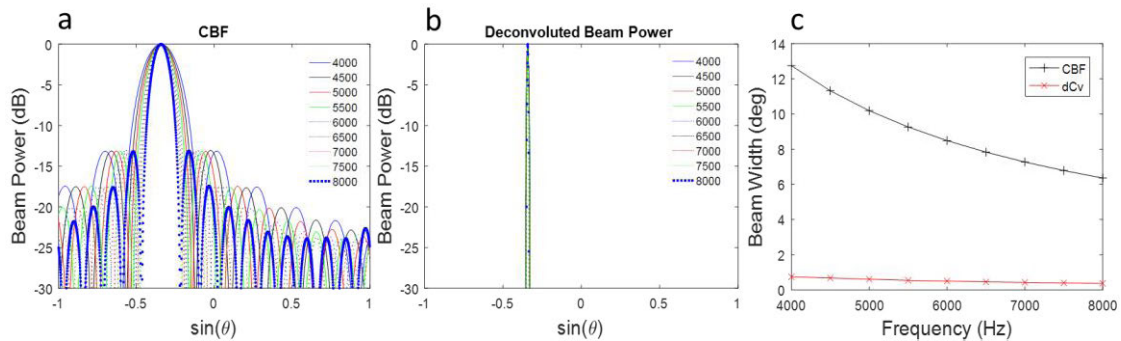
FIGURE 3. Beam patterns for a HLA of 16 elements using CBF (a) and deconvolved CBF (b) for frequencies from 4 to 8 kHz stepped by 500 Hz, and comparison of their 3 dB beamwidths (c). The array is cut for frequency at 8 kHz. For CBF in Fig. 3(a), lower frequencies have wider beams. For deconvolved CBF in Fig. 3(b), different frequencies have almost same beam width.

uniform array is approximately $0.89\lambda/L$ rad at broadside of the HLA [25], which yields $\sim 6.8°$ for an array of 16 element spaced at half-wavelength, see Fig. 3(a). This implies that the map resolution is poor in the cross-range direction (e.g., 83 m at a range of 700 m), consequently that the target is poorly localized. Second, CBF produces high sidelobes, which is translated to high reverberation levels since bottom reverberation comes from a wide area and sidelobes from one area feed into the level in another area. To improve the beam resolution and suppress the sidelobes, one needs high resolution beamforming methods, such as the well-known minimum variance distortionless response (MVDR) method. In this paper, we shall use the deconvolution method which has the advantage that the response is linear (as opposed to the nonlinear high resolution methods) since linearity is critical for the estimation of the scattering function. [Deconvolved CBF has been shown to be more robust than MVDR in [18].]

The deconvolution method starts with the CBF beam power for a given frequency. Deconvolving the CBF beam power yields a narrow beam width for a small array (Figures. 3(b) and 3(c)), equivalent to that of conventional array with a length order of magnitude longer and produces a sidelobe level 30 or more dB lower than that of CBF [18]. This technology is useful for object localization and separation of target from clutter and will be demonstrated in Sec. III using simulated data, and in Sec. IV using data collected in a tank.

[The concept and implementation of the method can be briefly summarized as follows. The CBF beam power can be expressed as the convolution of the beam pattern, Bp($\sin\phi - \sin\varphi$) with the source distribution $S(\sin\varphi)$, namely, $B_{\text{CBF}}(\sin\phi) = \int_{-\pi}^{\pi} \text{Bp}(\sin\phi - \sin\varphi)S(\sin\varphi)d(\sin\varphi)$. Deconvolution is a method to estimate source signal distribution given the CBF beam output and beam pattern [18]. We use the Richardson-Lucy (R-L) algorithm [26], [27], which is a Bayesian-based iterative method. The deconvolution is carried in the intensity domain and is well-conditioned (stable and known to converge) to a unique solution when all variables in the equation are positive [18]. The solution is denoted as $B_{\text{dCv}}(\sin\varphi)$. Sonar equation covers all angles (as opposed to limited view in astronomical image processing),

consequently, there is no ambiguity in reaching the final solution. The readers are referred to [18] for details.

Having separated the targets from clutter, one can improve the target to reverberation/background ratio by spatial averaging of the localization maps over multiple pings. It is experimentally known and theoretically expected that different bottom areas are ensonified by the source as the source or receiver moves (due to the changing eigenrays), so will the clutter (bottom facets) that are ensonified by the source. This means that the dominant clutter/reverberation appear at different locations as the source/receiver moves. (See data presented in Sec. IV.) Focusing on the target, the target echo level remains relatively the same unless the incident/outgoing angle changes significantly. Consequently, the targets will be enhanced by summing the localization map over multiple pings. This is demonstrated with tank data in Sec. IV.

III. SIMULATIONS

In this section, we study localization of underwater targets using simulated data. We assume a shallow water waveguide of a depth of 20 m, with a constant sound speed profile, overlaying a bottom. Two kinds of bottoms are considered here, one with a compressional sound speed of 1550 m/s and an attenuation coefficient of 10 dB/λ, and the other with a compressional sound speed of 1750 m/s and an attenuation coefficient of 0.2 dB/λ, both with a density of 1.5 g/cm^3. Because the bottom attenuation affects significantly transmission loss (TL) and the multi-paths time spread, we study how the bottom (attenuation) affects the localization performance. As discussed below, the duration of the direct blast (from the source to the receiver) determines the area where targets are not detectable. The echo level is dependent on the TL from the source to the target and target to the receiver. As an example, the beam time series based on data received on a HLA is shown in Fig. 4(a) and 4(b) (in dB) for high and low bottom attenuation respectively. Details are given below. One observes that, first, the echo return lasts about 0.01 s in Fig. 4(a) and about 4-5 times longer in Fig. 4(b). This is because many of the (late) multipath arrivals are being attenuated by the high bottom attenuation in Fig. 4(a).
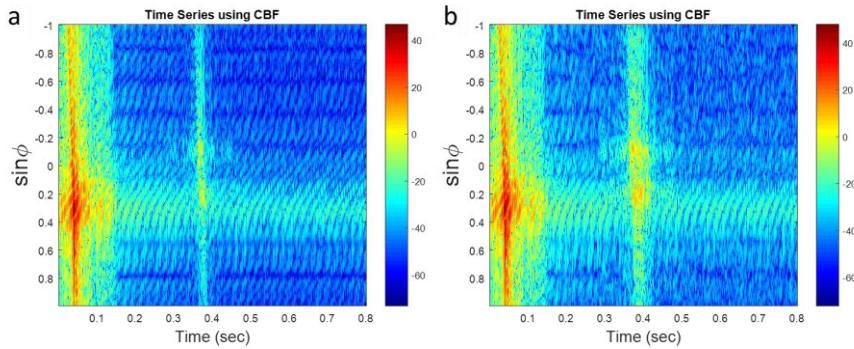
FIGURE 4. Simulated CBF beam time series (in dB) showing the arrival of direct blast (time ∼0.042 s) and echo returns from two targets (time ∼0.38 s) in an environment with (a) high and (b) low bottom attenuation.

TABLE 1. Simulation parameters.

	Source	Receiver	Water depth	Bottom		Source signal	Noise	Target property and position
Case I Towed HLA	x = -600 m, y = 0 m, z = 6 m	16 hydrophones, spaced at 1 m, depth 6 m, towed in a circle of radius 700 m	20 m	High attenuation 10 dB/λ	Low attenuation 0.2 dB/λ	LFM 400-800 Hz, duration 100 ms	No noise	Hard spheres of radius 0.5 m, located at (0 m, 0 m, 10 m), and (200 m, 200 m, 10 m)
Case II Fixed HLA	x = 0 m, y = 160.3 m, z = 6 m	16 hydrophones, spaced at 1 m, located at (x = 20 m, y= 110 m, z = 6 m)	20 m	High attenuation 10 dB/λ	Low attenuation 0.2 dB/λ	LFM 400-800 Hz, duration 100 ms	Echo to noise ratio 10 dB	Hard spheres of radius 0.5 m, located at (51 m, 402.9 m, 10 m), and (-46.2 m, 402.9 m, 10 m)

Second, the direct blast (from the source to the HLA) lasts about 0.2 s and has a sidelobe level higher than the echo level. In Fig. 4, the echo returns arrive at ∼0.38 s and are well separated from the direct blast. The echo returns will be hard to detect if they arrive with time less than 0.2 s.

The simulations are done for two cases. One for a fixed source and moving/towed HLA and the other with distributed sources and a fixed HLA. The simulation parameters are given in Table 1.

A. CASE I. TOWED HLA

The geometry is shown in Fig. 1(a). A target is located at the center of the coordinate. The source is located 600 m from the target. The HLA travels around the target in a circle with a radius of 700 m. We model the signal using the environment mentioned above. Both the source and HLA are deployed at a depth of 6 m. The target is a hard sphere of radius 0.5 m, deployed at a depth of 10 m. The source transmits a linear frequency modulated (LFM) signal from 400 Hz to 800 Hz with a duration 100 ms. The HLA contains 16 hydrophones, spaced at ∼ 1 m. The field scattered by target, received at the HLA is modeled according to (4). The data on the HLA are beamformed at 36 positions of the HLA, stepped 10 degrees counter clockwise from the nearest position to the source.

Data processing used is triangulation of beams from HLA at different positions as is commonly used for passive sonar. Here we extend the method to active sonar returns using simulated signals based on (4). Using CBF for target localization, the first requirement is that the target must not be masked by

the direct blast; or the target must arrive later than the direct blast (of duration 0.2 s). For the present case, only HLA at positions 1 to 11 and 27 to 36 meet this requirement; the corresponding data are referred to as ping 1-11 and 27-36. More pings could be included if the source-to-target and/or target-to-receiver ranges are extended.

To study the resolution of localization, we conduct the study without noise; the effect of the noise is to increase the background level without affecting the conclusions unless the signal-to-noise ratio is small or becomes negative. For the bottom of high attenuation, given that the echo duration is 0.01 s, the beamformed echo return are shown in Fig. 5(a) for the first ping. It shows a resolution wide in cross range and narrow in range as expected, because CBF produces a wide beam and has high sidelobes. The beamformed echo returns averaged over pings 1 to 5 are shown in Fig. 5(b). The beamformed echo returns averaged over pings 1-11 is shown in Fig. 5(c), and that averaged over pings 1-11 and 27-36 are shown in Fig. 5(d). It is apparent that the localization resolution improves with increasing number of pings. By averaging/summing maps over many (11, or 21) pings, one finds that the sidelobes are reduced and the main lobe is narrowed. This is because the final resolution is determined by the smaller of the along-range and cross-range resolutions. For the present case, the along range resolution, given by the product of the sound speed times the echo length (0.01s), is approximately 15 m, which is much less than the resolution in cross range determined by the product or range with the beam width, which is ∼83 m for this array as
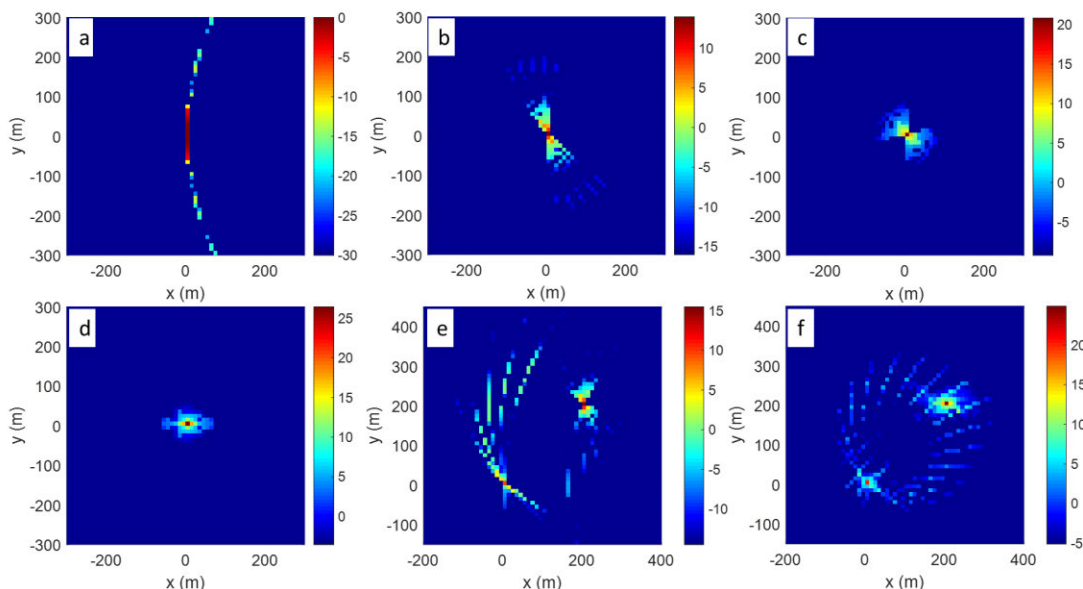
FIGURE 5. Localization map of one target using the first ping (a), pings 1-5 (b), pings 1-11 (c), and pings 1-11 and 27-36 (d), where each ping is received by the HLA at different scattering angle, stepped every 10 degrees. Localization map of two targets using pings 1-6 (e), and pings 1-6 and 27-36 (f).

mentioned in Sec. II. The improvement in localization using multiple pings comes from beam triangulation (assuming no timing error) yielding a resolution close to 15 m × 15m.

Next, consider the case of two targets, where the second target is located 200 m east and 200 m north of the first target as shown in Fig. 5(e) and (f). Figures 5(e) and (f) shows a localization map of two targets with 6 and 16 pings respectively. Similar to the case of one target, the side lobes are suppressed with increasing numbers of pings. One observes that, first, the sidelobes of the localization are different for different targets depending on the bearings of the HLA relative to the targets, and second, if there exist (high) clutter in the neighborhood of the target (within a few degrees), the target and clutter may not be distinguishable due to existence of high sidelobes.

For the case of low bottom attenuation, the echo pulse length is 4-5 times longer, which is translated into a localization area 3-4 time larger. In this case, the final resolution in localization is 60 m × 60 m or larger.

B. CASE 2. FIXED HLA
The source-receiver geometry is shown in Fig. 1(b). A HLA containing 16 hydrophones, spaced at $\sim$ 1 m, is deployed at 6 m below the surface at (x$\sim$20 m, y$\sim$110 m). The source is, in this case, moving. For this simulation, we shall consider one source located at (x = 0, y = 160.3 m). There are two targets (hard spheres of radius $\sim$0.5 m) located at (x = 51 m, y = 402.9 m), and (x = −46.2 m, y = 402.9 m), separated from the HLA by a range of approximately 300 m. See Fig. 6 for their locations.

The source transmits a linear frequency modulated (LFM) signal from 400 Hz to 800 Hz with a duration 100 ms. We calculate the pressure field from the source to each target and the HLA using (4), and summed up the pressure fields over

targets. We then add white noise. This is the received data. The received pressure field are inverse Fourier transformed to obtain the time series for each receiver. The time series are beamformed (e.g., by delay and sum) to obtain the beam times series which are plotted in dB in Fig. 4(a) for the high attenuation bottom and Fig. 4(b) for the low attenuation bottom. The beam time series are divided into overlapping blocks with 75% overlap, each of 256 samples (duration 25.6 ms) to estimate the beam energy (of each block) as a function of the beam angle and time, often referred to as the bearing-time record (BTR). The BTR is next transformed into a beam energy versus angle and range expressed in the Cartesian coordinate, referred to as localization map as shown in Fig. 6(a) for the high attenuation bottom and Fig. 6(c) for the low attenuation bottom. The noise level is adjusted so that the echo to noise/reverberation ratio (as seen in Figs. 6(a) and 6(c)) is about 10 dB. As is well known, the direct blast creates an area of ellipse shape around the source and receiver where targets within this area are difficult to detect. This area is about the same for the bottom with high attenuation, Fig. 6(a) or low attenuation, Fig. 6(c). One observes in Fig. 6(a) and 6(c) that the source creates a strong beam along the north-west direction. There also exists a strong beam along the south-west direction, which is the back lobe of the source beam due to left-right ambiguity of the HLA. The two targets are localized but with a poor resolution due to the wide beam width of CBF, similar to that shown in Fig. 5(a).

To process the data using deconvolved CBF, each block of data is Fourier transformed into the frequency domain. The R-L algorithm is applied to the beam power as a function of angle for each frequency. The dCv beam power is next summed over all frequencies (in the signal band) to obtain the BTR for the deconvolved CBF. The dCv BTR are
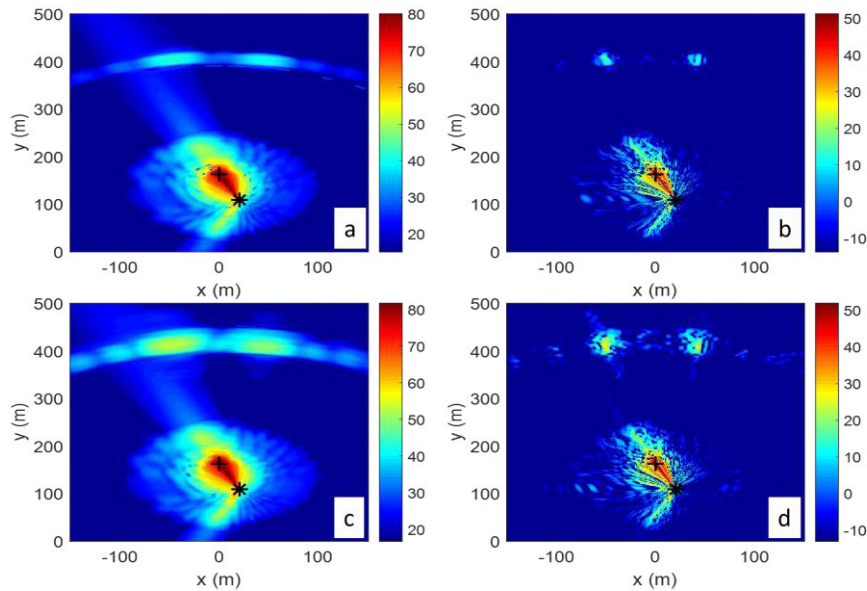
FIGURE 6. Localization result using simulated data. The receiver is located at (x~20 m, y~110 m) and the source is at (x=0, y =160.3 m). Beam energy as a function of angle and range, displayed in terms of the Cartesian coordinate, using CBF (a) and deconvolved CBF (b) for high attenuation bottom, and CBF (c) and deconvolved CBF (d) for low attenuation bottom.

transformed into a beam energy versus angle and range map in Cartesian coordinate. The dCv localization map is shown in Fig. 6(b) for the high attenuation bottom and 6(d) for the low attenuation bottom. One observes in this case, the two targets are well localized, with just one ping of data, due to the pencil-like beam of dCv. For the low attenuation bottom, the targets occupy a bigger area (less well localized) due to the many more multipath arrivals (longer echo duration) as mentioned above. There seems to be more (discrete) side-lobes in Fig. 6(d) than in Fig. 6(b) around the targets. This is likely due to that the multipath arrivals are coherent while the R-L algorithm assumes incoherent arrivals.

Note that the above simulations included the direct blast, echo returns and noise (or smooth reverberation) but no clutter returns (or discrete strong scattering returns from bottom facets). It is noted that clutter returns are dependent on the specifics of the bottom topology, and (very) difficult to simulate since the bottom topology is generally not known. On the other hand, clutter plays an important role in target localization. In real data analysis, clutter can often confuse the targets and presents a serious problem. We will illustrate how to solve this problem (separating echo from clutter) using the experimental results in Sec. IV.

It is also noted that while the above simulations were conducted at low frequencies, the results can be extended to high frequencies by scaling spatial dimension relative to wavelength without losing generality. [We use low frequency signals since the normal mode are well supported at low frequencies.] The purpose of the above simulation is to illustrate the signal processing. For a specific problem, one can conduct simulation using a propagation of one's choice to obtain detailed predictions.

IV. EXPERIMENTAL DATA ANALYSIS

In this section, target localization is demonstrated for two targets using experimental data collected in a tank with an estimated reflection coefficient of 0.25. The tank is 50 m long, 15 m wide and 10 m deep. Due to the shallow depth, it was observed that the multipaths were not easily separated in time. The experimental layout for the sources, two targets and the HLA is shown in Fig. 7(a). Figure 7(b) shows the photos of individual equipment (not to the scale). A water-filled metal spherical shell with a diameter of 50 cm is located at one side of the tank at (x = 5.2 m, y = 40.29 m), and a plastic sphere with a diameter 25 cm is placed at the opposite side (see Fig. 7(a)) (x = −4.62 m, y = 40.29 m). Both of them are submerged at 5 m depth. There was also an unintended target at (x = 0, y = 40.29 m) at the surface which turns out to produce high echo returns as discussed below. (The target strength (TS) of the water-filled metal spherical shell with a diameter of 50 cm is estimated to be approximately −26dB, and the TS of the cluster of plastic spheres of a diameter of 25cm is estimated to be close to −30dB based on experimental measurements. The unintended target in the middle has a TS similar to that of the metal shell.) The HLA has 16 hydrophones, spaced at 0.1 m, and is mounted at a rigid bar, 3 meters below the water surface located at (x = 1.25-2.75 m, y = 10.91 m). A source is placed at 8 positions at (x = 0, y = 16.29-37.29 m), equally-spaced along the y-axis, to obtain measurements at different incident angles to the targets. The source is also located at 3 m depth. It is noted that it is difficult to tow a HLA in a tank environment, thus we move the source and keep the HLA at a fixed position. The sound speed in the tank is measured at 1476 m/s. A 4-8 KHz LFM chirp signal with 0.01 s duration is

TABLE 2. Experimental parameters.

| Source: 8 positions, depth 3 m	Receiver	Environment	Source signal	Reverberation	Target I	Target II
P1: x=0, y =16.29 m P2: x=0, y =19.29 m P3: x=0, y =22.29 m P4: x=0, y =25.29 m P5: x=0, y =28.29 m P6: x=0, y =31.29 m P7: x=0, y =34.29 m P8: x=0, y =37.29 m	Fixed HLA (16 hydrophones, spaced at 0.1 m), x =1.25-2.75 m, y =10.91 m, z = 3 m.	Tank reflection coefficient 0.25, Water Depth 10 m, Isovelocity: 1476 m/s.	LFM 4-8 kHz, duration 10 ms	Exists, and varies with the source position	Target strength -26 dB, at (5.2 m, 40.29 m, 5 m)	Target strength -30 dB, at (-4.62 m, 40.29 m, 5 m)
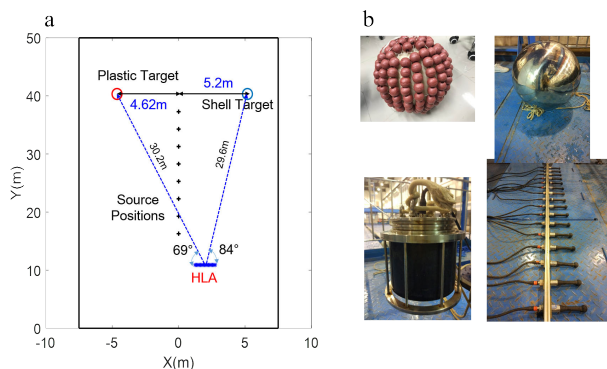
FIGURE 7. (a) Experimental layout of eight source positions, two target positions and the HLA position. (b) Photos of two targets (top row), and source and receiving HLA (bottom row) not scaled to actual sizes.

transmitted from the source and the data are collected on the HLA. The signal response with no presence of target is measured as the background field. The experimental parameters are given in Table 2.

Examples of the data and processing results are shown here for data transmitted by the source at the closest position to the HLA, located at (x = 0, y = 16.3 m). First, the raw data are pulse compressed by match filtering the received data for each ping with the transmitted LFM chirp. The signal energy of the matched filtered time series is shown in Fig. 8(a) as a function of (delay) time for each channel, and the corresponding spectrum is shown in Fig. 8(b). The received signal spectrum is not flat within the frequency band due to the transducer response. The target echo returns are not easily identified in Fig. 8(a).

Next the time series is beamformed to obtain the beam time series as a function of steering angle and delay time for each ping. One can use the delay and sum method, or perform the beamforming in the frequency domain and inverse Fourier transform the data to the time domain. The latter is used here for higher fidelity. The sample energy of the beamformed time series is shown in Fig. 9(a). The solid curves lines are scattering returns from the side walls of the tank. Besides these two relatively strong returns, one also observes other high level reverberations. The right side panel focuses on where the target echoes are expected (at time ~0.044 s) based on the known target locations. One observes the echoes but they are not well separated in beam angle. The returns at

~0.053 s are reflections from the wall at the other end of the tank.

The beam time series are divided into 50% overlapping segments each 0.0013 s long. The energy of each segment is summed and displayed as a function of time in Fig. 10(a). This has the effect of smoothing the reverberation returns without significantly affecting echo returns. The beam energy versus angle and time is transformed into angle and distance and displayed in terms of the Cartesian coordinate (x, y), as shown in Fig. 10(b). One observes the elliptic structure of the direct blast from the source to the receiver and reverberation from the bottom near the source and receivers. The echo returns from the targets are more clearly seen in this beam energy time display (the rectangle in Fig. 10(a) and circles in Fig. 10(b)), but the returns from the targets are not separated in angle due to the poor resolution of the HLA using CBF. The targets are not well localized in Fig. 10(b).

In order to improve the localization result with a higher resolution, we apply deconvolution to the CBF beam outputs. The beam data in each segment is zero padded and Fourier transformed into the frequency domain to obtain finer frequency bins. Deconvolution is applied to the beam energy (as a function of beam angle) for each frequency components. The deconvolved CBF (dCv) outputs are summed over frequency for each segment and then displayed as a function of time and angle. We used the Rechardson-Lucy algorithm with 200 iterations [28]. The dCv beam energy versus angle and time is shown in Fig. 11(a) based on data from the source at position 1, which is next transformed into beam energy versus angle and range, displayed in terms of the Cartesian coordinate, the localization map, in Fig. 11(b). One observes that: (1) the echo and reverberation returns are more discretely distributed in Fig. 11 compared with Fig. 10, (2) the returns from the two targets are (well) separated in the beam domain, (3) there is strong reverberation return along the bearing of the source, and (4) Fig. 11(b) displays a lower level of background noise plus reverberation relative to the direct blast signal than Fig. 10(b). Figure 11 appears more "speckled" compared with Fig. 10. This is expected for narrow beam sonar which is able to resolve individual returns better.

To compare clutter returns for sources at different positions, we show in Fig. 11(d) the dCv beam energy versus angle and time, and in Fig. 11(e) the dCv localization map
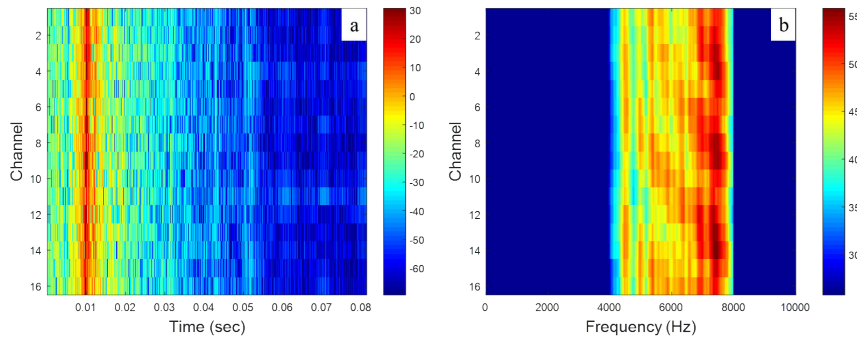
FIGURE 8. (a) Signal energy received on the HLA as a function of delay time. Echo returns from the scatterers are not easily identified. (b) Signal spectrum for individual channels.
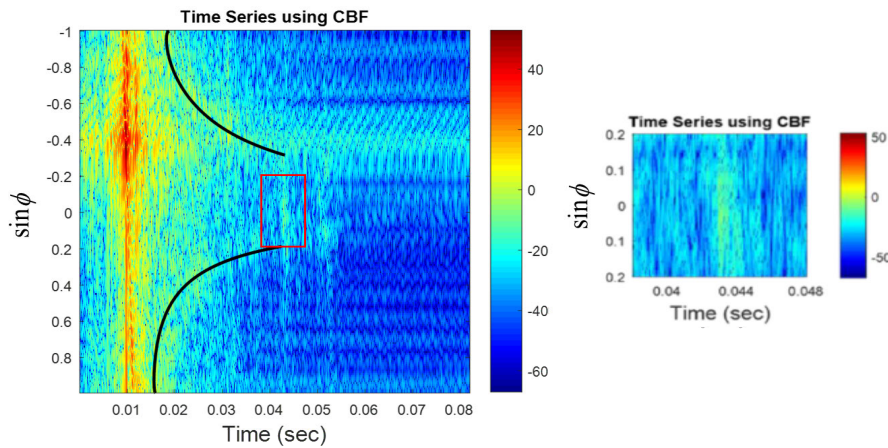

FIGURE 9. Beam time sample energy as a function of steering angle and delay time based on the beam time series; angle measured from the broadside of the HLA (left). The curved lines show the scattering returns from the tank walls. Zoomed-in display focusing on the target echoes is shown on the right. The deconvolution is done in terms of sine of the bearing angle as described in the text.
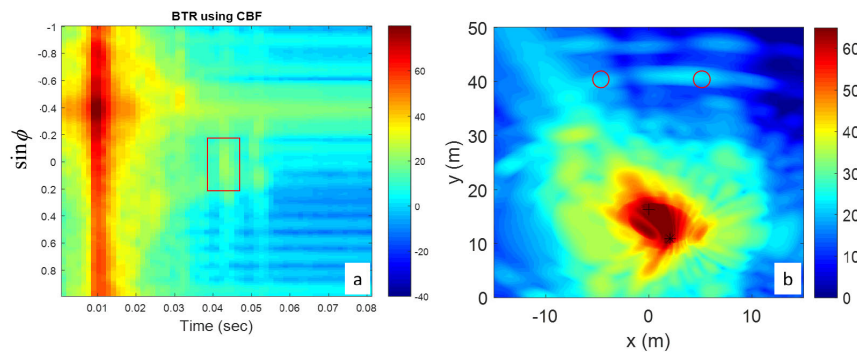

FIGURE 10. (a) Beam energy time series, while the beam energy is averaged over short time windows of Fig. 7. (b) Beam energy as a function of angle and range, displayed in terms of the Cartesian coordinate. The receiver is located at (x~2 m, y~11 m) and the source is at (x=0, y=16.3 m). The red circles denote the actual positions of the two targets.

in Cartesian coordinate based on data from the source at position 4 (x = 0, y = 25.3 m). One observes that the reverberation maps (the location of the dominant reverberation) are different for sources at different positions (compare Fig. 11(b) with 11(e)). The reason is that sources at different positions are known to ensonify different bottom

areas relative to the receiver. Consequently, the dominant reverberation/clutter will show up at different locations for different source positions as seen in Fig. 11(b) and 1(c). The target echo level changes slowly (due to different TL) as the source moves, unless the sound incidence angle at the target changes substantially. One observes that the targets are
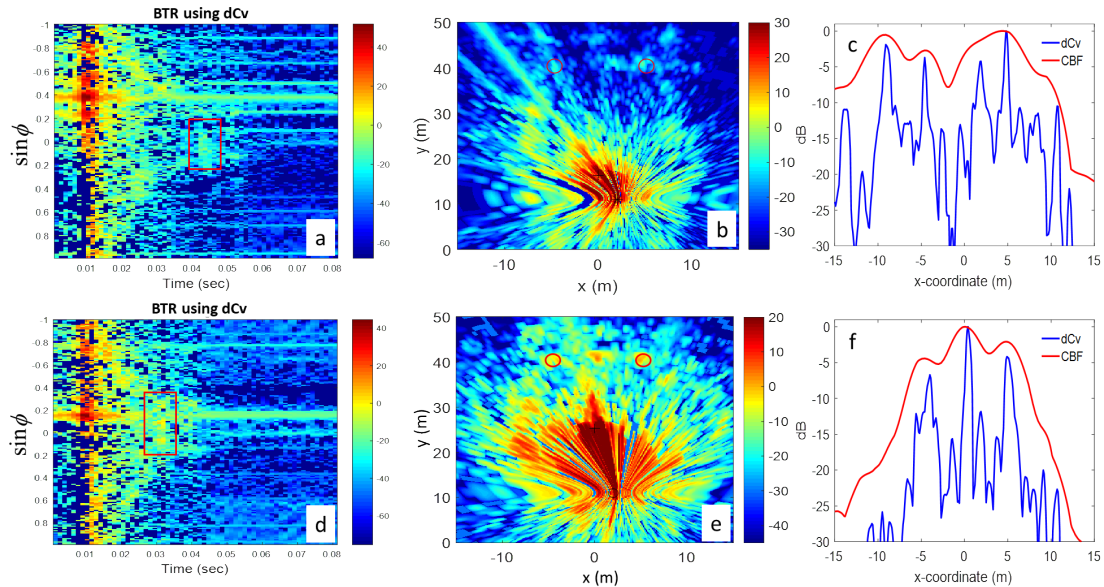
FIGURE 11. (a) and (d) The beam energy as a function of time using deconvolved CBF with 200 iterations. (b) and (e) Targets localization in Cartesian coordinate (x, y) using deconvolved CBF. (c) and (f) The normalized beam energy along the x axis at y = 40.29 m based on data in (b) and (e) respectively. (a), (b) and (c) are for source at position 1, and (d), (e) and (f) are for source at position 4. The red circles denote the actual positions of the two targets.
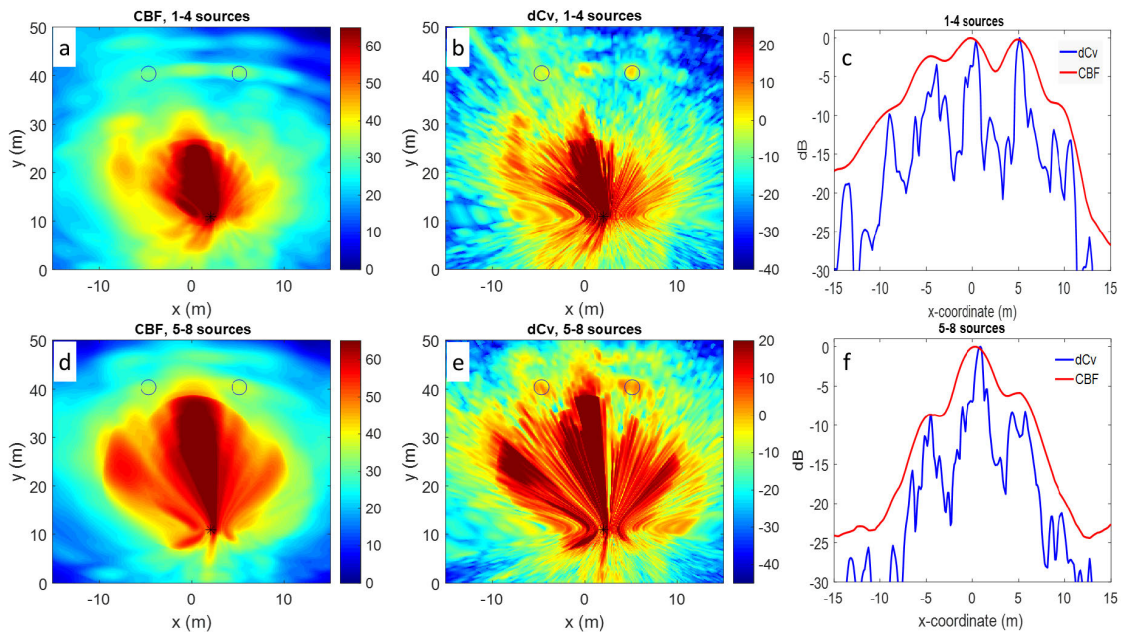

FIGURE 12. Targets localization in Cartesian coordinate (x, y) using CBF (a) and (d) and deconvolved CBF (b) and (e). (a)-(c) summing over pings from 1-4 source positions. (d)-(f) summing over pings from 5-8 source positions. (c) and (f) normalized beam energy along x axis cut at y = 40.29 m.

seen in Fig. 11(e) but not easily identifiable in Fig. 11(b). Figures 11(c) and 11(f) shows the relative beam energy along the x-axis at y = 40.29 m.

The beam map (x, y) plots are created from data from the source at 8 different locations using one ping for each case. It is anticipated that reverberation/clutters from difference sources will be different, and hence by summing/averaging the map from different sources, reverberation/clutter may be suppressed. Figure 12(a) and 12(b) show the beam map (x, y) plot averaged over the first four sources at locations (x = 0, y = 16.29-25.29 m). One observes that, compared with the map of one ping, Fig. 11(b), the reverberation near the targets are suppressed and the two targets are well localized in Fig. 12(b). Figure 12(c) compared the intensity at the line y = 40.29 m using CBF and dCv. One finds a peak-to-background (or target to reverberation/noise) ratio on the

order of ∼4 dB for CBF and ∼15 dB for dCv for the two targets at x = 5.2 m and −4.6 m. (The background level is measured in the neighborhood of the target, in areas not contaminated by other targets.) Similarly, we average the beam (x, y) maps over 4 sources located at (x = 0, y = 28.29-37.29 m) located further away from the HLA. The results are shown in Fig. 12(d) and 12(e) using CBF and dCv respectively. The area of direct blast and bottom reverberation is larger in Fig. 12(d) and (e) than in Fig. 12(a) and 12(b) due to the fact that the source ensonifies a bigger bottom area in the forward propagation direction. Nonetheless, the two targets are clearly localized in Fig. 12(e). Figure 12(c) and (f) shows a peak-to-background (target-to-reverberation/noise) ratio on the order of ∼5 dB for CBF and ∼20 dB for dCv. When reverberations appear at different locations as the source moves, the average reverberation level (over an area outside of the target) tends to decrease by averaging over different sources.

In Fig. 12(b) and 12(e), one observes a strong echo return from an object at (x ∼ 0 m and y ∼ 40 m) with a slightly stronger scattering strength than that of the two targets (see Fig. 12(c) and 12(f)). The is the unintended target mentioned above, and is found to be a tile laying on the water surface (under the instrument rack) with cones protruding into the water to a depth of ∼ 0.2-0.3 m. The results show that surface target can also be well localized using the proposed method.

The above experimental localization (map) results can perhaps be understood by comparing them with the simulation results presented in Sec. III. While the simulations were done using low frequency 400-800 Hz signals and data were collected using high frequency 4-8 kHz signals, they can be compared by scaling the source, target, receiver configuration by the ratio of frequencies, i.e., 10; the source, target and source geometry in the simulations in Sec. III was purposely set up by this rule for the purpose of comparing them with experimental results. [We use low frequency signals in Sec. III since the normal mode calculation has been well verified at low frequencies.] Indeed, one finds the experimental localization result using CBF, Fig. 10(b), is similar to that obtained with simulated data, Fig. 6(a) except for a scale factor of 10. Obviously, the experimental result, Fig. 10(b), contains many clutter returns and an additional unintended target, which are absent in the simulation results Fig. 6(a). Also the echo levels in the data are somewhat lower than in the simulation. These two factors make it more difficult to identify/localize the target in the data than in the simulation. Likewise, the experimental results using deconvolved CBF, Fig. 11(b) is quite similar to the simulation result presented in Fig. 6(b), except for the clutter returns. The clutter returns are more discrete and this helps to localize the target and enhance the target to reverberation/background ratio as demonstrated above.

V. SUMMARY AND CONCLUSION

This paper investigates the ability of a bistatic active system consisting of a fixed source and moving HLA, and vice versa, to localize the targets within the viewing area. Targets can be localized by beamforming on the active returns and triangulation of multiple beams from a towed HLA assuming no timing error, but localization becomes difficult using conventional beamforming when there exist high level reverberation/clutter returns as the echo and reverberation are not well separated in the beam domain when the array does not have sufficient beam resolution as is for an AUV towed array. We solve this problem using deconvolved CBF as it achieves high beam resolution and low sidelobe level equivalent to that of a much (10 times) larger HLA, thus avoiding the use of synthetic beamforming (which yields no more than approximately twice the aperture of the original HLA) and the uncertainties associated with array element localization [18]. Localization of targets is further improved by summing the target map over many pings as the source or the HLA travels over different places to provide a large azimuthal angle coverage. Localization of two targets are demonstrated by the tank experimental data using the proposed method.

REFERENCES

[1] J. R. Edwards, H. Schmidt, and K. D. LePage, "Bistatic synthetic aperture target detection and imaging with an AUV," *IEEE J. Ocean. Eng.*, vol. 26, no. 4, pp. 690–699, Oct. 2001.

[2] K. D. LePage and H. Schmidt, "Bistatic synthetic aperture imaging of proud and buried targets from an AUV," *IEEE J. Ocean. Eng.*, vol. 27, no. 3, pp. 471–483, Jul. 2002.

[3] H. Schmidt and A. Balasuriya. (2012). *Multistatic, Concurrent Detection, Classification and Localization Concepts for Autonomous, Shallow Water Mine Counter Measures*. [Online]. Available: http://lamss.mit.edu/lamss/pmwiki/pmwiki.php?n=Site.Projects

[4] E. M. Fischell and H. Schmidt, "Classification of underwater targets from autonomous underwater vehicle sampled bistatic acoustic scattered fields," *J. Acoust. Soc. Amer.*, vol. 138, no. 6, pp. 3773–3784, Dec. 2015.

[5] A. Pan, J. Fan, and B. Wang, "Acoustic scattering from a double periodically bulkheaded and ribbed finite cylindrical shell," *J. Acoust. Soc. Amer.*, vol. 134, no. 5, pp. 3452–3463, Nov. 2013.

[6] D. S. Plotnick, P. L. Marston, K. L. Williams, and A. L. España, "High frequency backscattering by a solid cylinder with axis tilted relative to a nearby horizontal surface," *J. Acoust. Soc. Amer.*, vol. 137, no. 1, pp. 470–480, Jan. 2015.

[7] M. Zampolli, A. L. Espana, K. L. Williams, S. G. Kargl, E. I. Thorsos, J. L. Lopes, J. L. Kennedy, and P. L. Marston, "Low-to mid-frequency scattering from elastic objects on a sand sea floor: Simulation of frequency and aspect dependent structural echoes," *J. Comput. Acoust.*, vol. 20, no. 2, Jun. 2012, Art. no. 1240007.

[8] A. M. Gunderson, A. L. España, and P. L. Marston, "Spectral analysis of bistatic scattering from underwater elastic cylinders and spheres," *J. Acoust. Soc. Amer.*, vol. 142, no. 1, pp. 110–115, Jul. 2017.

[9] S. F. Morse, P. L. Marston, and G. Kaduchak, "High-frequency backscattering enhancements by thick finite cylindrical shells in water at oblique incidence: Experiments, interpretation, and calculations," *J. Acoust. Soc. Amer.*, vol. 103, no. 2, pp. 785–794, Aug. 1998.

[10] K. Baik, C. Dudley, and P. L. Marston, "Acoustic quasi-holographic images of scattering by vertical cylinders from one-dimensional bistatic scans," *J. Acoust. Soc. Amer.*, vol. 130, no. 6, pp. 3838–3851, Dec. 2011.

[11] B. H. Houston, J. A. Bucaro, and D. M. Photiadis, "Broadband acoustic scattering from a ribbed shell," *J. Acoust. Soc. Amer.*, vol. 98, no. 5, pp. 2851–2853, Oct. 1995.

[12] D. M. Photiadis, B. H. Houston, E. G. Williams, and J. A. Bucaro, "Resonant response of complex shell structures," *J. Acoust. Soc. Amer.*, vol. 108, no. 3, pp. 1027–1035, Aug. 2000.

[13] J. A. Bucaro, B. H. Houston, M. Saniga, L. R. Dragonette, T. Yoder, S. Dey, L. Kraus, and L. Carin, "Broadband acoustic scattering measurements of underwater unexploded ordnance (UXO)," *J. Acoust. Soc. Amer.*, vol. 123, vol. 2, pp. 738–746, Feb. 2008.

[14] J. A. Bucaro, H. Simpson, L. Kraus, L. R. Dragonette, T. Yoder, and B. H. Houston, "Bistatic scattering from submerged unexploded ordnance lying on a sediment," *J. Acoust. Soc. Amer.*, vol. 126, no. 5, pp. 2315–2323, Nov. 2009.

[15] K. L. Williams, S. G. Kargl, E. I. Thorsos, D. S. Burnett, J. L. Lopes, M. Zampolli, and P. L. Marston, "Acoustic scattering from a solid aluminum cylinder in contact with a sand sediment: Measurements, modeling, and interpretation," *J. Acoust. Soc. Amer.*, vol. 127, no. 6, pp. 3356–3371, Jun. 2010.

[16] S. G. Kargl, K. L. Williams, T. M. Marston, and J. L. Kennedy, "Acoustic response of unexploded ordnance (UXO) and cylindrical targets," in *Proc. IEEE OCEANS*, Seattle, WA, USA, Sep. 2010, pp. 1–5.

[17] W. Xu, F. Sun, S. Fan, and X. Pan, "A unified framework for multiple-input multiple-output and bistatic synthetic aperture sonar processing," in *Proc. IEEE OCEANS*, Genova, Italy, May 2015, pp. 1–4.

[18] T. C. Yang, "Deconvolved conventional beamforming for a horizontal line array," *IEEE J. Ocean. Eng.*, vol. 43, no. 1, pp. 160–172, Jan. 2018.

[19] T. C. Yang and T. Yates, "Scattering from an object in a stratified medium. I. Frequency dispersion and active localization," *J. Acoust. Soc. Amer.*, vol. 96, no. 2, pp. 1003–1019, Jun. 1994.

[20] M. Meyer and J.-P. Hermand, "Backpropagation techniques in ocean acoustic inversion: Time reversal, retrogation and adjoint model—A review," in *Acoustic Sensing Techniques for the Shallow Water Environment*. Dordrecht, The Netherlands: Springer, 2006.

[21] J. G. Minonzio, D. Clorennec, A. Aubry, T. Folegot, T. Pelican, C. Prada, J. de Rosny, and M. Fink, "Application of the DORT method to the detection and characterization of two targets in a shallow water waveguide," in *Proc. IEEE OCEANS*, Brest, France, Jun. 2005, pp. 1001–1006.

[22] X. Zeng, H. Ma, and H. Wang, "Localization performance under middle and low frequency sound source based on time reversal method in enclosed space," *IEEE Access*, vol. 7, pp. 5649–5661, Dec. 2018.

[23] F. Ingenito, "Scattering from an object in a stratified medium," *J. Acoust. Soc. Amer.*, vol. 82, no. 6, pp. 2051–2059, Dec. 1987.

[24] N. C. Makris, P. Ratilal, and Y. Lai, "Validity of the sonar equation and Babinet's principle for object scattering in a shallow water waveguide," *J. Acoust. Soc. Amer.*, vol. 106, no. 4, p. 2158, Aug. 1999.

[25] M. A. Richards, "Introduction to Radar Systems," in *Fundamentals of Radar Signal Processing*, 2nd ed. New York, NY, USA: McGraw-Hill, 2005, ch. 1, p. 12.

[26] W. H. Richardson, "Bayesian-based iterative method of image restoration," *J. Opt. Soc. Amer.*, vol. 62, no. 1, pp. 55–59, Jan. 1972.

[27] L. B. Lucy, "An iterative technique for the rectification of observed distributions," *Astronomical J.*, vol. 79, no. 6, pp. 745–754, Jun. 1974.

[28] D. Sun, C. Ma, T. C. Yang, J. Mei, and W. Shi, "Improving the performance of a vector sensor line array by deconvolution," *IEEE J. Ocean. Eng.*, to be published. doi: 10.1109/JOE.2019.2912586.

T. C. YANG received the Ph.D. degree in high energy physics from the University of Rochester, Rochester, NY, USA, in 1971. He was the Pao Yu-Kong Chair Professor with Zhejiang University. From 2012 to 2014, he was the National Science Counsel Chair Professor with the National Sun Yat-sen University, Kaohsiung, Taiwan. Before that, he spent 32 years working at the Naval Research Laboratory, Washington, DC, serving as the Head of the Arctic Section, Dispersive Wave Guide Effects Group, and an acting Head of the Acoustic Signal Processing Branch, and a Consultant to the division on research proposals. He is currently a Professor with Zhejiang University. His current research interests include array signal processing exploring super-directivity and super-gain and applications, environmental acoustic sensing and signal processing using distributed networked sensors, and methods for improved channel tracking and data-based source localization. In earlier years, he pioneered matched mode processing for a vertical line array, and matched-beam processing for a horizontal line array. Other areas of research include underwater acoustic communications, geoacoustic inversions, waveguide invariants, effects of internal waves on sound propagation in shallow water, and Arctic acoustics. He is also a Fellow of the Acoustical Society of America.

TING ZHANG received the B.E. degree in telecommunication engineering from the Beijing University of Posts and Telecommunications, Beijing, China, in 2007, the M.S. degree in signal and information processing from the Chinese Academy of Sciences, Beijing, China, in 2007, and the Ph.D. degree in optics, photonics, and image processing from Ecole Centrale Marseille, France, in 2014, respectively.

From 2014 to 2017, she has been a Postdoctoral Researcher with the Electronics and Electromagnetism Laboratory (L2N), Sorbonne University, and an Assistant Professor with Aix Marseille University. She has been currently an Assistant Professor with Zhejiang University, China, since July 2017. Her research interests include signal processing, underwater target localization and classification, and inverse scattering problems.

WEN XU (S'97–A'01–M'02–SM'04) received the B.E. degree in electrical engineering from the University of Science and Technology of China, Hefei, China, in 1990, the M.S. degree in acoustics from the Institute of Acoustics, Chinese Academy of Sciences, Beijing, China, in 1993, and the Ph.D. degree in oceanographic engineering from Massachusetts Institute of Technology (MIT), Cambridge, MA, USA, jointly with Woods Hole Oceanographic Institution, Woods Hole, MA, USA, in 2001.

From 1993 to 1996, he was a Research Engineer with the Institute of Acoustics, Chinese Academy of Sciences. He was a Research Scientist with the Ocean Acoustics Group, MIT, from 2001 to 2002, and a Research Scientist/Senior Research Scientist with the Teledyne RD Instruments, San Diego, CA, USA, from 2003 to 2007. He is currently a Professor with the College of Information Science and Electronic Engineering, Zhejiang University, Hangzhou, China. His research interests include statistical and array signal processing in general and in applications to sonar, radar, and communication systems, and most recently to underwater sensor networks. He has been an Associate Editor for the IEEE JOURNAL OF OCEANIC ENGINEERING, since 2010, and an Editorial Board Member for the *Chinese Journal of Acoustics*.

● ● ●